Supplementary Information (SI) for Inorganic Chemistry Frontiers.
This journal is © the Partner Organisations 2025

Electronic Supplementary Material (ESI) for Inorganic Chemistry Frontiers

Supporting Information

Constructing 3D crosslinked CeO_2 nanosheet/graphene architectures anchored with Pd nanoparticles for boosted formic acid and methanol oxidation performance

Cuizhen Yang[a,b,c], Tingyao Wang[a,b], Tianyi Wang[a,b], Hao Yuan[a,b], Hongxing Li[c], Haiyan He[d], Dongming Liu[a,b],*, Huajie Huang[d],*

aSchool of Materials Science and Engineering, Anhui University of Technology, Maanshan, Anhui 243002, China

bAnhui Province Key Laboratory of Efficient Conversion and Solid-State Storage of Hydrogen & Electricity, Anhui University of Technology, Maanshan, Anhui 243002, China

cAnhui Xinchuang Energy Conservation and Environmental Protection Technology Co. Ltd, Maanshan, Anhui 243002, China

dCollege of Materials Science and Engineering, Hohai University, Nanjing 210098, China

**E-mail addresses: huanghuajie@hhu.edu.cn or ldm_ahut@163.com*

Contents

1. Figures

Fig. S8. Raman spectra of Pd/CeO_2. The F_{2g} Raman band is a symmetric Ce-O vibrational mode with a distinct ceria oxide Raman peak.

Fig. S9. EDX spectrum of the 3D Pd/CeO_2-G architecture confirms the co-existence of C, O, Ce and Pd components in the material. Since the sample was held on a Cu grid, Cu peaks were also detected.

Fig. S10. EPR spectra for Pd/CeO_2-G and Pd/CeO_2. There is an obvious symmetrical peak at approximately g ~ 2.003 in Pd/CeO_2-G, which is a typical oxygen vacancy peak.

Fig. S11. Pd 3d spectra of Pd/CeO_2-G and Pd/G samples, showing that the binding energies for both metallic Pd and Pd^{2+} peaks of Pd/CeO_2-G are shifted actively compared with those of Pd/G.

Fig. S12. (a) LSV curves and (b) corresponding Tafel plots at 0.5 V of the Pd/CeO_2-G architectures with varying CeO_2/G ratios electrodes in 0.5 mol L^{-1} H_2SO_4 and 0.5 mol L^{-1} HCOOH solution at 50 mV s^{-1}, showing that the formic acid oxidation reaction is much easier to take place on the Pd/CeO_2-G(5:5).

Fig. S13. The stability characteristics of different catalysts in methanol oxidation. (a) Cycling stability comparison of Pd/CeO_2-G(5:5), Pd/CeO_2, Pd/G, Pd/CNT, and Pd/C. Results from 500 consecutive cycle scans of methanol oxidation in 0.5 mol L^{-1} H_2SO_4 and 0.5 mol L^{-1} HCOOH for (b) Pd/CeO_2-G(5:5), (c) Pd/CeO_2, (d) Pd/G, (e) Pd/CNT, and (f) Pd/C catalysts, highlighting the superior cycling stability of Pd/CeO_2-G(5:5).

Fig. S14. (a) The CV curves of the Pd/CeO_2-G(5:5) before and after 5000 cycles in 0.5 mol L^{-1} H_2SO_4 and 0.5 mol L^{-1} HCOOH. and (b) the formic acid oxidation mass activities of Pd/CeO_2-G(5:5) before and after the cycling tests.

Fig. S15. (a) LSV curves and (b) corresponding Tafel plots at 0.5 V of the Pd/CeO_2-G architectures with varying CeO_2/G ratios electrodes in 0.5 mol L^{-1} NaOH and 1 mol L^{-1} CH_3OH solution at 50 mV s^{-1}, showing that the formic acid oxidation reaction is much easier to take place on the Pd/CeO_2-G(5:5).

Fig. S16. ECSA-normalized CV curves of the Pd/CeO_2-G(5:5), Pd/CeO_2, Pd/G, Pd/CNT in 0.5 mol L^{-1} NaOH and 1 mol L^{-1} CH_3OH.

Fig. S17. The stability characteristics of different catalysts in methanol oxidation. (a) Cycling stability comparison of Pd/CeO_2-G(5:5), Pd/CeO_2, Pd/G, Pd/CNT, and Pd/C. Results from 1000 consecutive cycle scans of methanol oxidation in 0.5 mol L^{-1} NaOH and 1 mol L^{-1} CH_3OH for (b) Pd/CeO_2-G(5:5), (c) Pd/CeO_2, (d) Pd/G, (e) Pd/CNT, and (f) Pd/C catalysts, highlighting the superior cycling stability of Pd/CeO_2-G(5:5).

Fig. S18. Typical (a-b) SEM and (c) TEM and (d) HRTEM images of the Pd/CeO_2-G nanoarchitecture after the long-term chronoamperometric test.

Fig.S19. Relaxed atomic structures for the CO adsorption on (a) Pd/G and (b)Pd-CeO_2 models, further confirming the enhanced anti-poisoning capability of Pd when supported on CeO_2.

Table S1. Compiled study comparing CV results for different catalysts.

Table S2. Comparison of methanol oxidation behavior on the Pd/CeO_2-G(5:5) composite and various Pd-based electrocatalysts.

Table S3. The charge-transfer resistance (R_{ct}) of different catalysts.

1. Figures

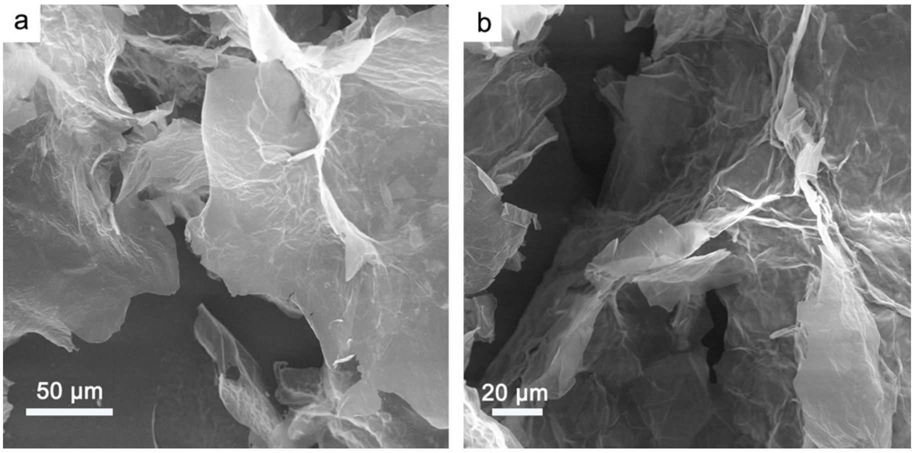

Fig. S1. Representative SEM images of (a, b) GO nanosheets, respectively, revealing the 2D lamellar structure of GO nanosheets.

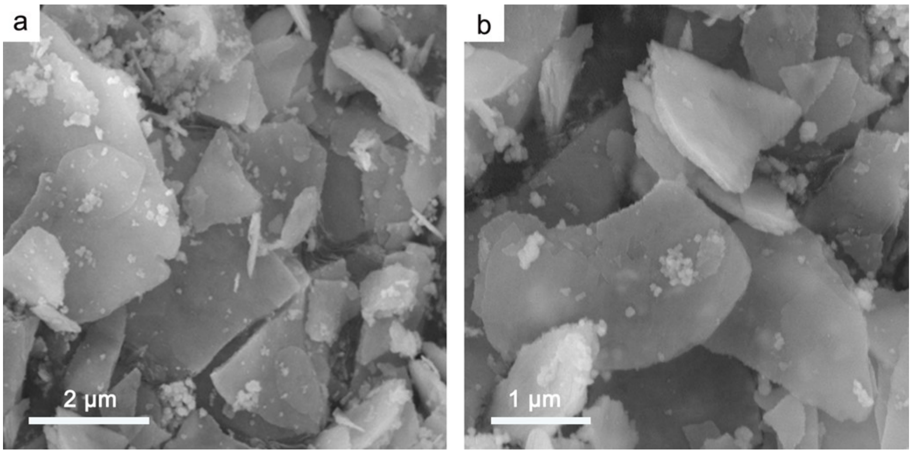

Fig. S2. Representative SEM images of (a, b) CeO_2 nanosheets, respectively, revealing the lamellar structure of the CeO_2.

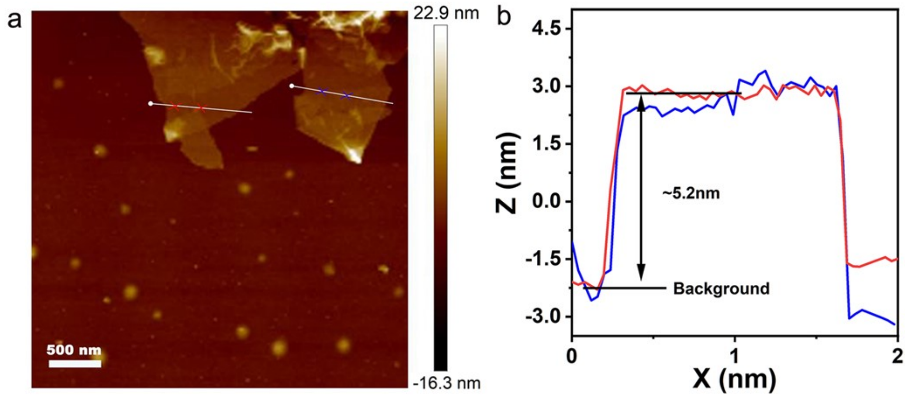

Fig. S3. (a) Representative AFM image of the CeO_2 nanosheets. (b) Based on the examination of the white lines, a thorough thickness analysis reveals that the CeO_2 nanosheets exhibit a consistent thickness of approximately 5.2 nm.

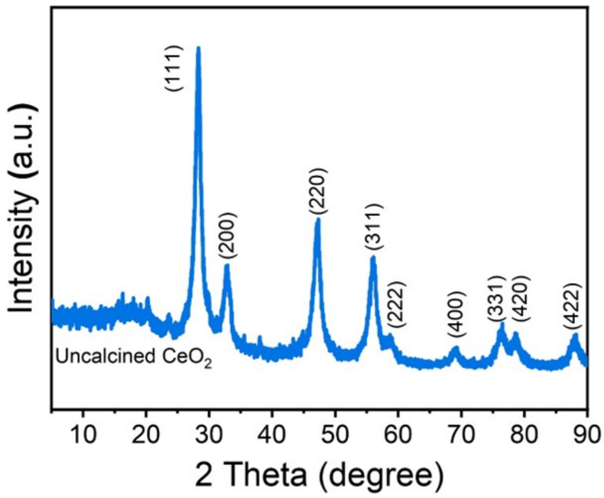

Fig. S4. The XRD patterns of uncalcined CeO_2 nanosheets, suggesting that the uncalcined CeO2 nanosheets have impurities.

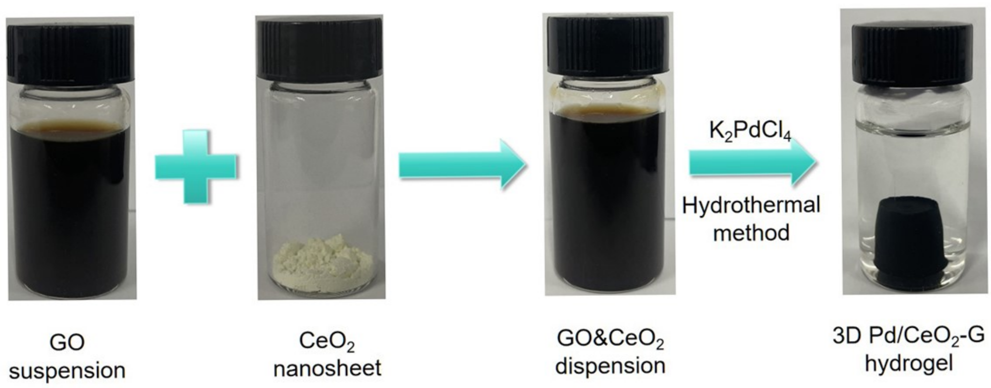

Fig. S5. The synthetic process for the 3D Pd/CeO_2-G hydrogels. It includes: (1) mixture CeO_2 and GO suspension via an ultrasonic treatment; (2) formation of 3D Pd/CeO_2-G hydrogel through a solvothermal reaction.

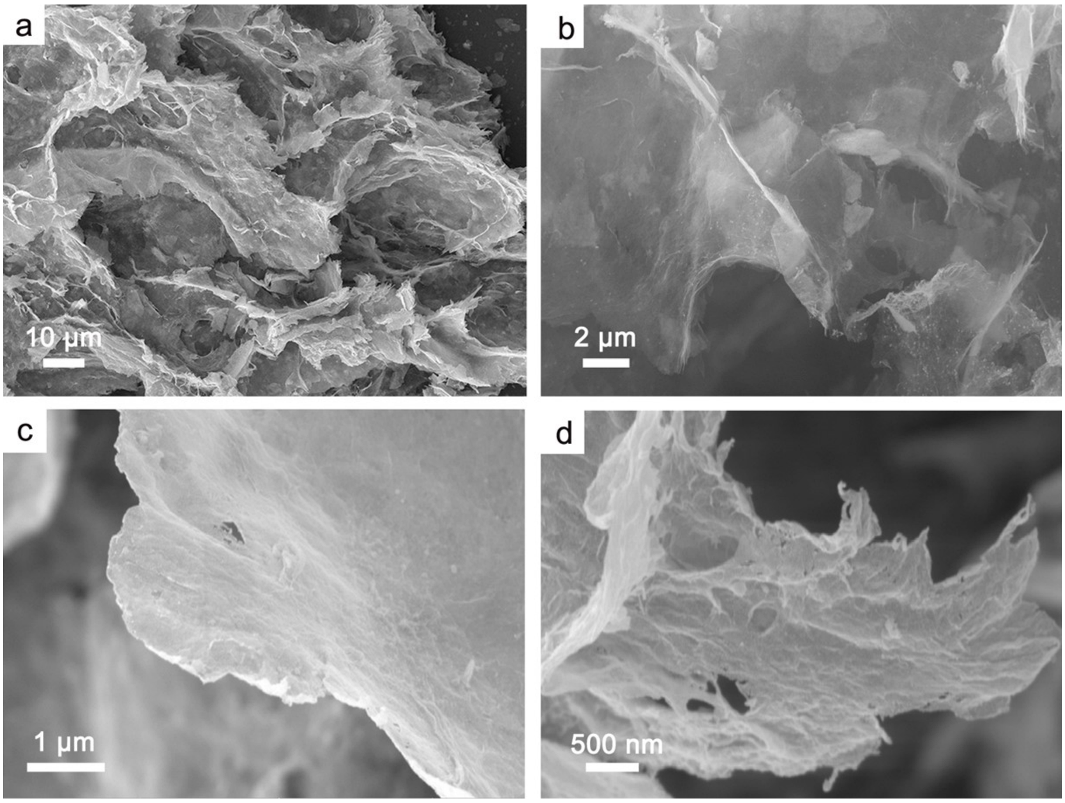

Fig. S6. FE-SEM images of the 3D Pd/CeO_2-G architecture at different magnifications. (a, b) Low-magnification FE-SEM images indicate that the material has numerous well-defined macropores. (c, d) High-magnification FE-SEM images focused on CeO_2 and graphene regions, respectively, showing distribution of Pd NPs on the surfaces.

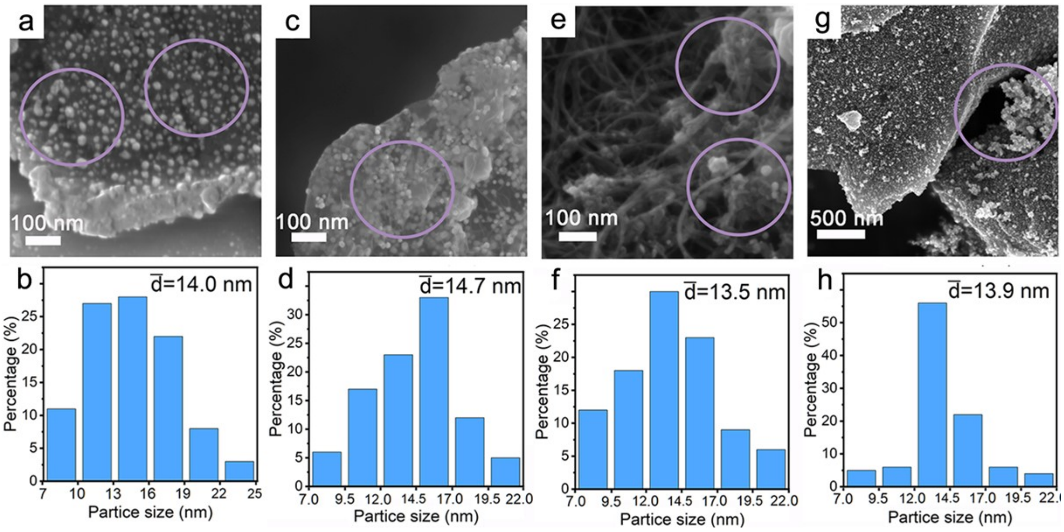

Fig. S7. FE-SEM images and Pd particle size distribution of (a, b) Pd/CeO_2, (c, d) Pd/G, (e, F) Pd/CNT, and (g, h) Pd/C, respectively, revealing that Pd NPs are easy to form aggregates in these samples, as pointed out by the circles.

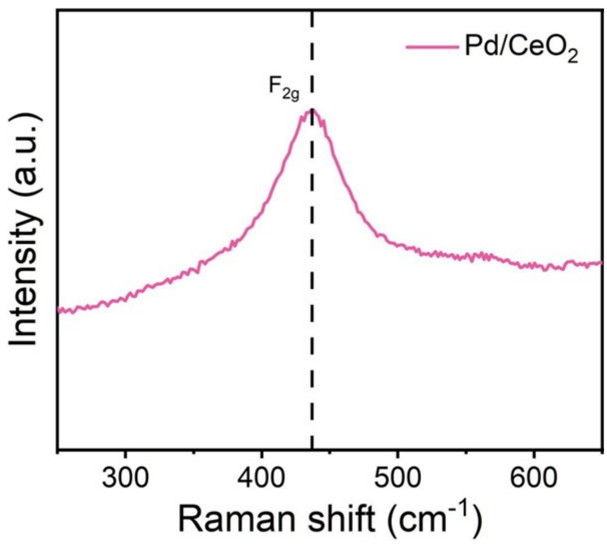

Fig. S8. Raman spectra of Pd/CeO_2. The F_{2g} Raman band is a symmetric Ce-O vibrational mode with a distinct ceria oxide Raman peak.

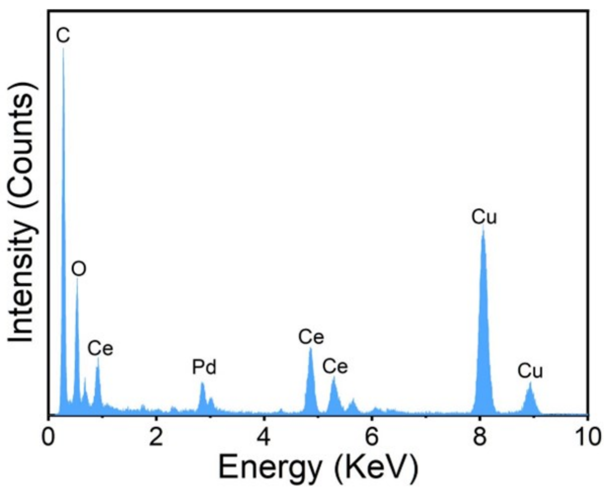

Fig. S9. EDX spectrum of the 3D Pd/CeO_2-G architecture confirms the co-existence of C, O, Ce and Pd components in the material. Since the sample was held on a Cu grid, Cu peaks were also detected.

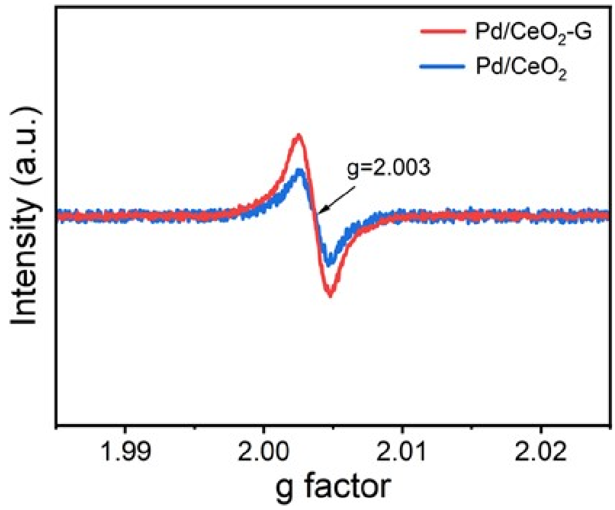

Fig. S10. EPR spectra for Pd/CeO_2-G and Pd/CeO_2. There is an obvious symmetrical peak at approximately g ~2.003 in Pd/CeO_2-G, which is a typical oxygen vacancy peak.

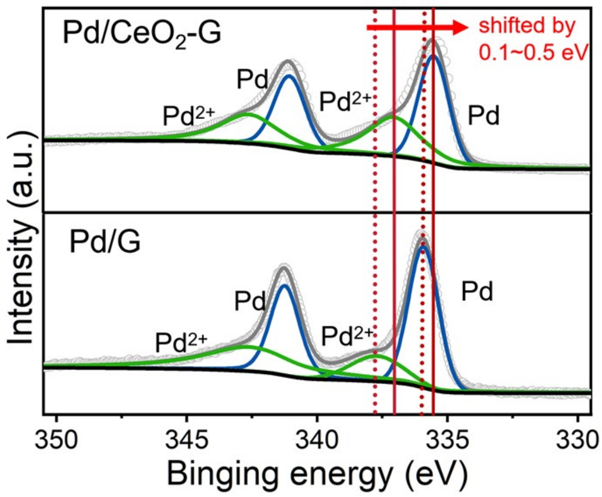

Fig. S11. Pd 3d spectra of Pd/CeO_2-G and Pd/G samples, showing that the binding energies for both metallic Pd and Pd^{2+} peaks of Pd/CeO_2-G are shifted actively compared with those of Pd/G.

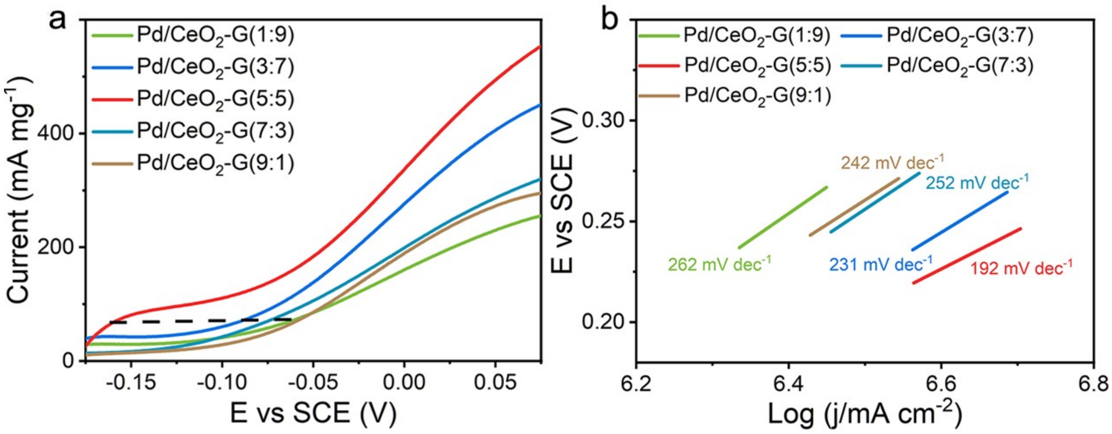

Fig. S12. (a) LSV curves and (b) corresponding Tafel plots at 0.5 V of the Pd/CeO_2-G architectures with varying CeO_2/G ratios electrodes in 0.5 mol L^{-1} H_2SO_4 and 0.5 mol L^{-1} HCOOH solution at 50 mV s^{-1}, showing that the formic acid oxidation reaction is much easier to take place on the Pd/CeO_2-G(5:5).

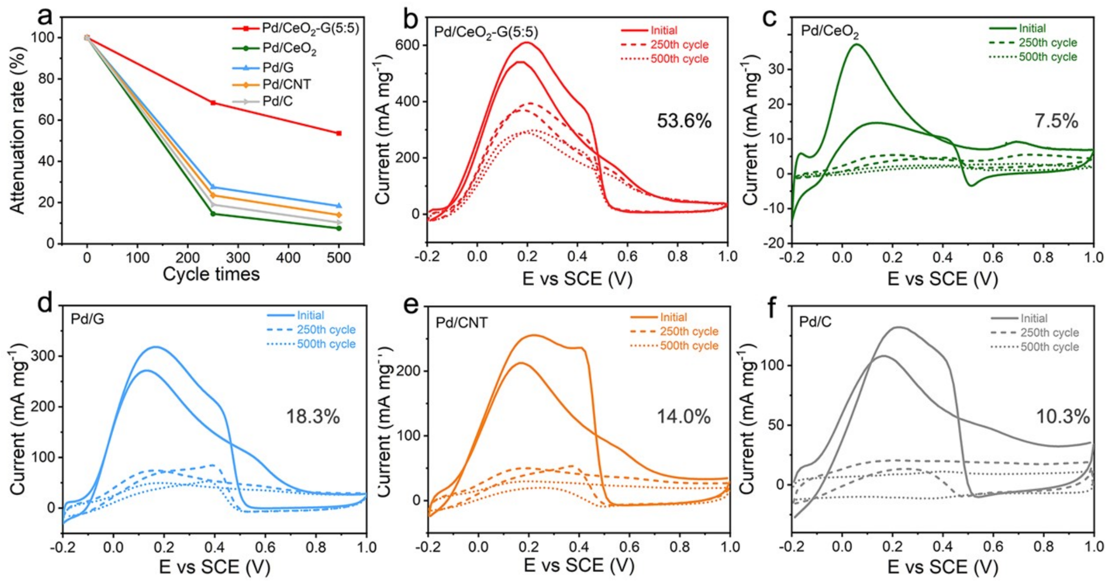

Fig. S13. The stability characteristics of different catalysts in formic acid oxidation. (a) Cycling stability comparison of Pd/CeO_2-G(5:5), Pd/CeO_2, Pd/G, Pd/CNT, and Pd/C. Results from 500 consecutive cycle scans of methanol oxidation in 0.5 mol L^{-1} H_2SO_4 and 0.5 mol L^{-1} HCOOH for (b) Pd/CeO_2-G(5:5), (c) Pd/CeO_2, (d) Pd/G, (e) Pd/CNT, and (f) Pd/C catalysts, highlighting the superior cycling stability of Pd/CeO_2-G(5:5).

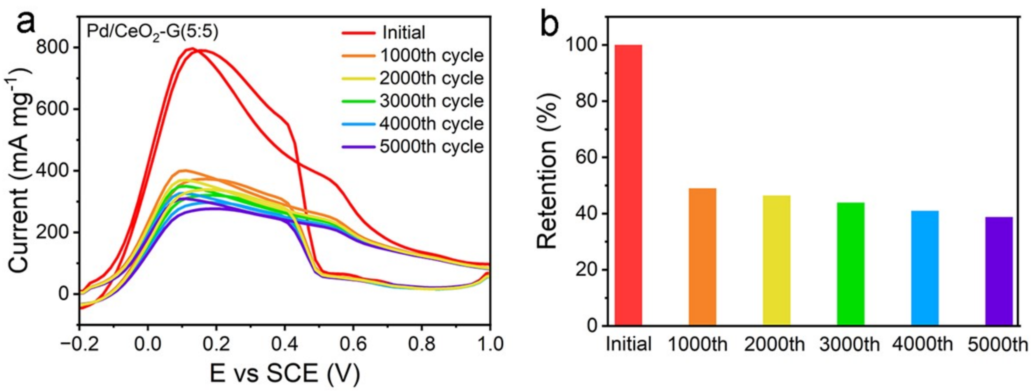

Fig. S14. (a) The CV curves of the Pd/CeO_2-G(5:5) before and after 5000 cycles in 0.5 mol L^{-1} H_2SO_4 and 0.5 mol L^{-1} HCOOH. and (b) the formic acid oxidation mass activities of Pd/CeO_2-G(5:5) before and after the cycling tests.

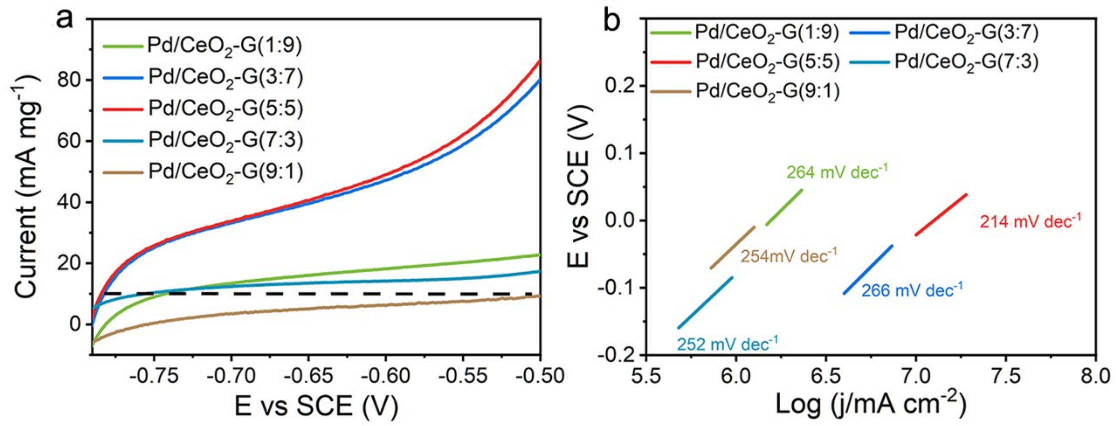

Fig. S15. (a) LSV curves and (b) corresponding Tafel plots at 0.5 V of the Pd/CeO_2-G architectures with varying CeO_2/G ratios electrodes in 0.5 mol L^{-1} NaOH and 1 mol L^{-1} CH_3OH solution at 50 mV s^{-1}, showing that the formic acid oxidation reaction is much easier to take place on the Pd/CeO_2-G(5:5).

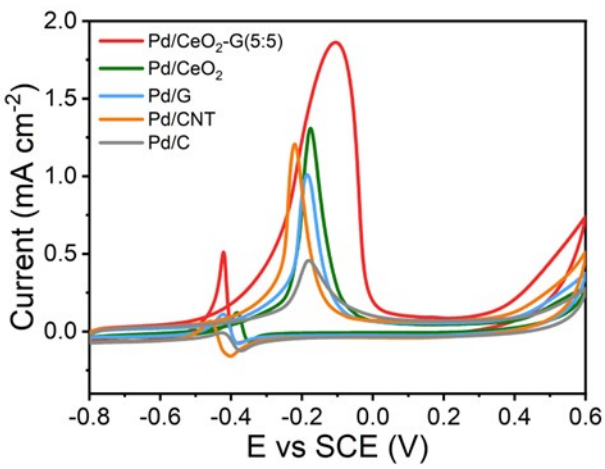

Fig. S16. ECSA-normalized CV curves of the Pd/CeO_2-G(5:5), Pd/CeO_2, Pd/G, Pd/CNT in 0.5 mol L^{-1} NaOH and 1 mol L^{-1} CH_3OH.

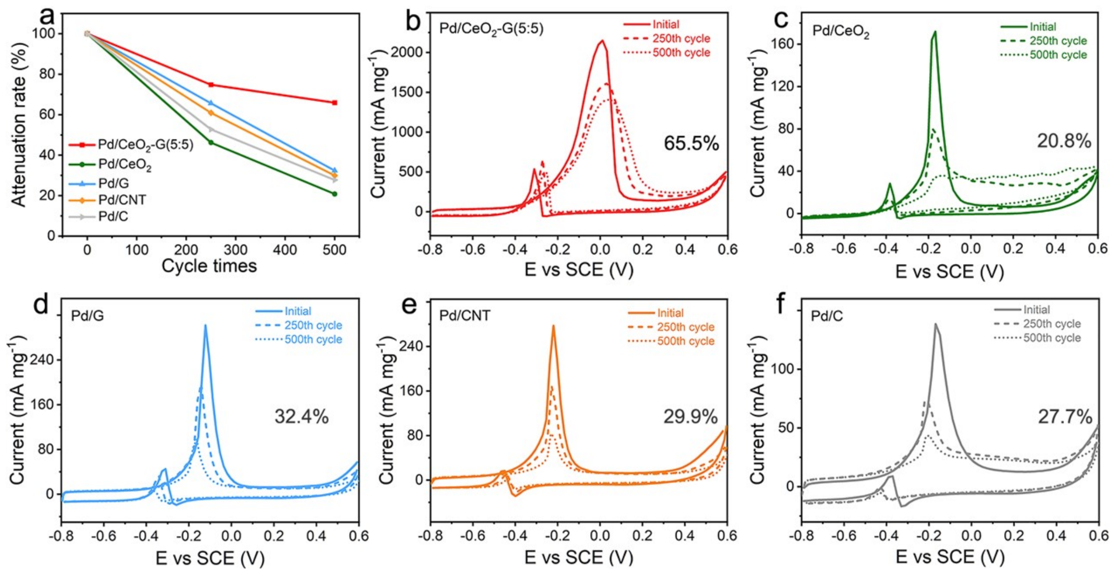

Fig. S17. The stability characteristics of different catalysts in methanol oxidation. (a) Cycling stability comparison of Pd/CeO_2-G(5:5), Pd/CeO_2, Pd/G, Pd/CNT, and Pd/C. Results from 500 consecutive cycle scans of methanol oxidation in 0.5 mol L^{-1} NaOH and 1 mol L^{-1} CH_3OH for (b) Pd/CeO_2-G(5:5), (c) Pd/CeO_2, (d) Pd/G, (e) Pd/CNT, and (f) Pd/C catalysts, highlighting the superior cycling stability of Pd/CeO_2-G(5:5).

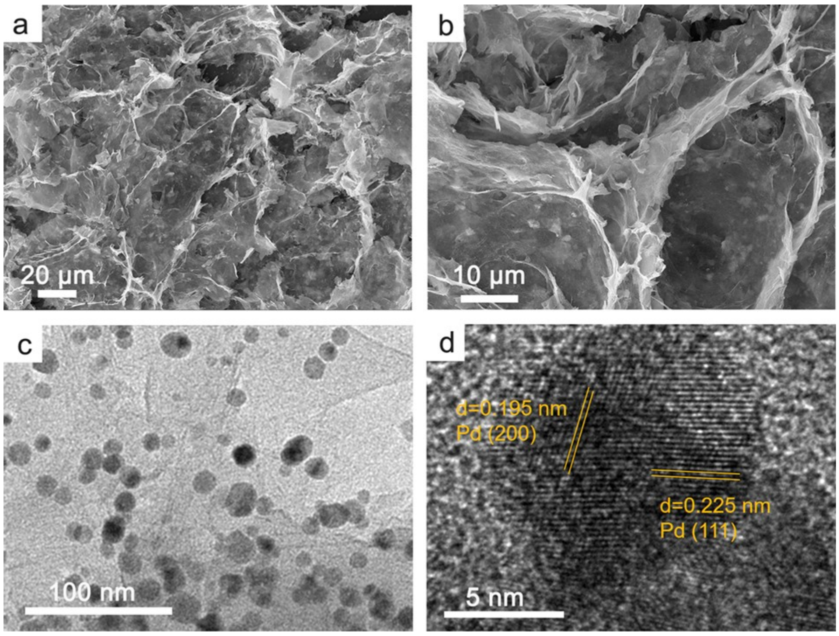

Fig. S18. Typical (a-b) SEM and (c) TEM and (d) HRTEM images of the Pd/CeO_2-G nanoarchitecture after the long-term chronoamperometric test.

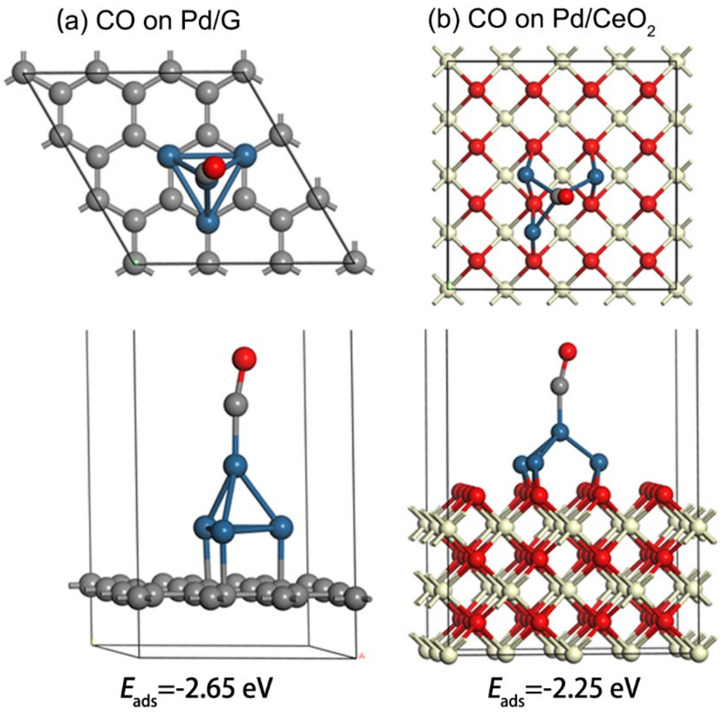

Fig.S19. Relaxed atomic structures for the CO adsorption on (a) Pd/G and (b)Pd-CeO_2 models, further confirming the enhanced anti-poisoning capability of Pd when supported on CeO_2.

Table S1. Compiled study comparing CV results for different catalysts.

Electrode	ECSA ($m^2\ g^{-1}$)		Mass activity ($mA\ mg^{-1}$)		Specific activity ($mA\ cm^{-2}$)	
	DFAFC	DMFC	DFAFC	DMFC	DFAFC	DMFC
Pd/CeO_2-G(1:9)	37.5	43.6	276.8	415.2	7.8	11.8
Pd/CeO_2-G(3:7)	84.7	91.7	502.0	1773.0	14.2	50.2
Pd/CeO_2-G(5:5)	107.9	115.8	681.0	2143.5	19.3	60.7
Pd/CeO_2-G(7:3)	47.1	58.5	372.1	563.0	10.5	15.9
Pd/CeO_2-G(9:1)	30.7	37.8	300.3	498.8	8.5	14.1
Pd/CeO_2	8.5	12.7	54.5	166.0	1.5	4.7
Pd/G	28.6	35.0	245.0	353.0	6.9	10.0
Pd/CNT	23.1	20.1	200.0	242.5	5.7	6.9
Pd/C	18.2	17.0	124.5	138.5	3.5	3.9

Table S2. Comparison of methanol oxidation behavior on the Pd/CeO_2-G(5:5) composite and various Pd-based electrocatalysts.

Catalyst	ECSA ($m^2\ g^{-1}$)	Mass activity ($mA\ mg^{-1}$)	Scan rate ($mV\ s^{-1}$)	Electrolyte	Reference
Pd/CeO_2-G(5:5)	107.9	681.0	50	0.5 M H_2SO_4 + 0.5 M HCOOH	This work
	115.8	2143.5	50	0.5 M NaOH + 1 M CH_3OH	
PtPd/GO	38.0	924.0	50	1 M KOH + 0.5 M CH_3OH	[1]
Pd-Cu-Co/GO	47.1	1062.5	50	1 M KOH + 1 M CH_3OH	[2]
Pd-Mo_2N/GO	51.5	532.7	50	0.5 M H_2SO_4 + 0.5 M HCOOH	[3]
Pd/BN-GO	43.4	1141.7	50	1 M KOH + 1 M CH_3OH	[4]
Pd/BNG	82.1	707.5	50	0.5 M NaOH + 1 M CH_3OH	[5]
Pd/NS-GO	83.4	501.8	50	0.5 M H_2SO_4 + 0.5 M HCOOH	[6]
Pd/PPy-GO	69.4	1192.7	50	1 M KOH + 1 M CH_3OH	[7]
Pd/$CoMoO_4$-modified graphene	50.5	1109.3	50	1 M KOH + 1 M CH_3OH	[8]
Pd/DPHE-GO	54.8	1539.0	50	1 M KOH + 1 M CH_3OH	[9]
Pd/MCNTs	68.3	402	50	0.5 M H_2SO_4 + 0.5 M HCOOH	[10]
PdCuSn/CNTs	N.A.	395.9	50	1 M KOH + 0.5 M CH_3OH	[11]
Pd/NG-CNT	88.8	1396.0	50	0.5 M NaOH + 1 M CH_3OH	[12]

Table S3. The charge-transfer resistance (Rct) of different catalysts.

Electrode	R_{ct}	
	Value (ohm)	Error (%)
Pd/CeO_2-G(5:5)	17.6	6.1
Pd/G	32.6	8.7
Pd/CNT	38.7	4.8
Pd/C	2166.0	3.3

References

1 L. Xu, Q. Cui, H. Zhang, A. Jiao, Y. Tian, S. Li, H. Li, M. Chen, F. Chen, Ultra-clean PtPd nanoflowers loaded on GO supports with enhanced low-temperature electrocatalytic activity for fuel cells in harsh environment, Appl. Surf. Sci., 2020, **511**, 145603.

2 F. Yang, B. Zhang, S. Dong, C. Wang, A. Feng, X. Fan, Y. Li, Reduced graphene oxide supported Pd-Cu-Co trimetallic catalyst synthesis, characterization and methanol electrooxidation properties, J. Energy Chem., 2019, **29**, 72-78.

3 H. Yan, Y. Jiao, A. Wu, C. Tian, L. Wang, X. Zhang, H. Fu, Synergism of molybdenum nitride and palladium for high-efficiency formic acid electrooxidation, J. Mater. Chem. A, 2018, **6**, 7623-7630.

4 J. Shu, H. Ma, G. Tang, R. L, S. Ma, J. Meng, H. Yan, S. Li, Ultrafine oxygen ophilic nanoalloys induced by multifunctional interstitial boron for methanol oxidation reaction, J. Colloid Interface Sci., 2023, **629**, 482-491.

5 Y. Yang, H. Huang, B. Shen, L. Jin, Q. Jiang, L. Yang, H. He, Anchoring nanosized Pd on three-dimensional boron- and nitrogen-codoped graphene aerogels as a highly active multifunctional electrocatalyst for formic acid and methanol oxidation reactions, Inorg. Chem. Front., 2020, **7**, 700-708.

6 X. Zhang, J. Zhu, C. Tiwary, Z. Ma, H. Huang, J. Zhang, Z. Lu, W. Huang, Y. Wu, Palladium nanoparticles supported on nitrogen and sulfur dual-doped graphene as highly active electrocatalysts for formic acid and methanol oxidation, ACS Appl.

Mater. Interfaces, 2016, **8**, 10858-65.

7 S. Xie, L. Deng, H. Huang, J. Yuan, J. Xu, R. Yue, One-pot synthesis of porous Pd-polypyrrole/nitrogen-doped graphene nanocomposite as highly efficient catalyst for electrooxidation of alcohols, J. Colloid Interface Sci., 2022, **608**, 3130-3140.

8 N. Kumari, V. Srirapu, A. Kumar, R. Singh, Use of palladium nanoparticles dispersed on GNS-modified with 10 wt% $CoMoO_4$ as efficient bifunctional electrocatalysts, Int. J. Hydrogen Energy, 2019, **44**, 31312-31322.

9 S. Li, S. Ma, Y. Zhang, L. Zhao, H. Yang, R. Jin, Metal-organic interface engineering for coupling palladium nanocrystals over functionalized graphene as an advanced electrocatalyst of methanol and ethanol oxidation, J. Colloid Interface Sci., 2021, **588**, 384-392.

10 H. Zhao, T. Zhao, Highly active carbon nanotube-supported Pd electrocatalyst for oxidation of formic acid prepared by etching copper template method, Int. J. Hydrogen Energy, 2013, **38**, 1391-1396.

11 F. Zhu, G. Ma, Z. Bai, R. Hang, B. Tang, Z. Zhang, X. Wang, High activity of carbon nanotubes supported binary and ternary Pd-based catalysts for methanol, ethanol and formic acid electro-oxidation, J. Power Sources, 2013, **242**, 610-620.

12 J. Ren, J. Zhang, C. Yang, Y. Yang, Y. Zhang, F. Yang, R. Ma, L. Yang, H. He, H. Huang, Pd nanocrystals anchored on 3D hybrid architectures constructed from nitrogen-doped graphene and low-defect carbon nanotube as high-performance multifunctional electrocatalysts for formic acid and methanol oxidation, Mater.

Today Energy, 2020, **16**, 100409.